Structure Characterization Revisited

Charles Rino,

August 3, 2026

Abstract

This report is the third of a series addressing the theory of scintillation and diagnostic processing of electromagnetic EM wave transmissions that have traversed the ionosphere. Scintillation is a manifestation of EM propagation in transparent inhomogeneous media. The inhomogeneous structure includes quasi-deterministic and stochastic components, which are not cleanly separated. *Scintillation Theory Revisited* and *Phase Screen Models Revisited* are largely concerned with propagation theory, simulations and signal models with emphasis on diagnostic processing.

Structure Characterization Revisited reviews the characterization of stochastic ionospheric structure and how that characterization can be inferred from diagnostic measurements. Measurements are one-dimensional time series that respond to electron density integration along source-to-receiver paths. Motion of the propagation paths relative to the structure generates the observed time variation.

The conceptual picture of developed structure is a configuration of slowly evolving field-aligned striations. Propagation paths capture intercepted striations. Statistical structure is defined in planes that cut across striated field lines. In regions where the field-lines are locally parallel straigntforward geometric corrections define the intercepted structure. However, field-line curvature can distort the intercepted structure. The interpretation of diagnostic measurements must take into account where the structure originates and how it maps along field lines from *pierce points* to equatorial plane interceptions.

1 Introduction

High-resolution equatorial plasma bubble (EPB) simulations have been used to characterize the evolution of EPBs and ensuing structure development in unstable regions. Simulations are typically initiated with smoothly varying electron density profiles with imposed electric and magnetic fields. The electric fields generate $E \times B$ drifts. The induced electric potential that responds to perturbations on the bottom side of the layer can initiate upward propagating depletions referred to as a *plasma bubble.* Steepening upward gradients are unstable and ultimately create evolving stochastic structure. Dynamic equations that characterize the structure evolution can be solved numerically.

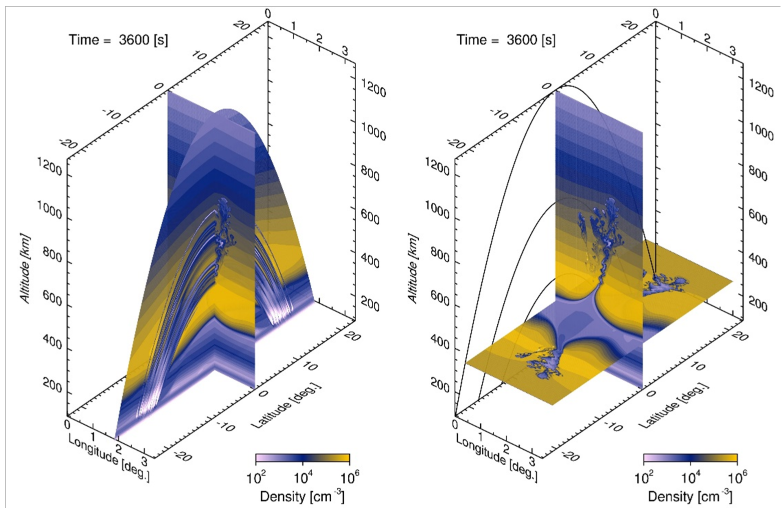

Figure 1: Physics-based high-resolution simulation in magnetic field coordinates. The meridional plane shown in the left-hand frame contains field lines. The equatorial plane shown in the right hand frame is perpendicular to field lines revealing the 2D scale distribution.

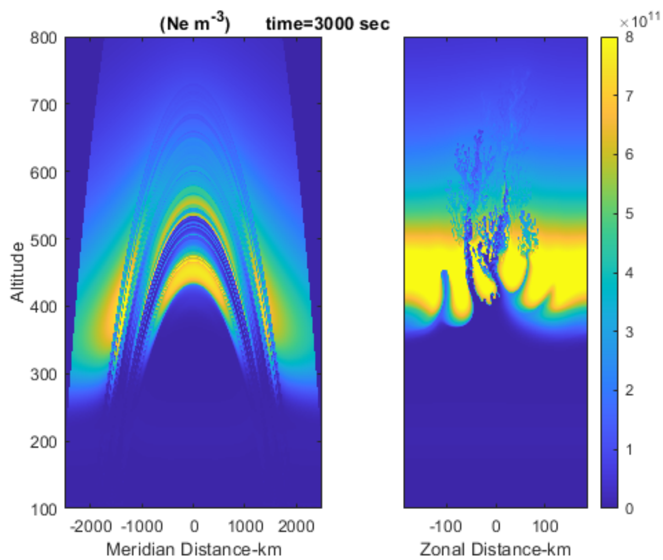

Figure 2: Interpolated rectangular coordinate display at 300 sec. Right frame shows equatoral EPB structure. Left frame shows meridional plane structure.

For computational efficiency the simulations are performed in an asymmetrically-sampled field-aligned coordinate system defined by a magnetic dipole offset in a spherical-earth model to approximate the earth's magnetic field. In the geomagnetic system evolving *striations* map symmetrically along magnetic field lines emanating from the equatorial plane. Figure 1 summarizes fully-developed three-dimensional structure from an EPB simulation generated by Yokoyama [1] and made available for this study.

The display coordinates in Figure 1 are geomagnetic latitude, longitude, and height above a spherical-earth surface. The left frame displays striated structure in the meriodinal plane. The right frame displays stochastic structure defined by striations intercepting the equatorial plane. Nonuniform sampling resolves structure to hundreds of meters. However, spectral analysis requires interpolation to uniformly sampled Cartesian coordinates. The left frame in Figure 2 shows interpolated meriodinal plane structure. The right frame in Figure 2 shows interpolated equatorial plane structure. The interpolated snapshots were captured at an earlier (300 sec) time. Although the two frames have equal height sampling and a common axis at $y = z = 0$, the y extent in the equatorial plane is much smaller than the z extent in the meriodinal plane. This asymmetry has ramifications for propagation paths penetrating the structure at arbitrary angles.

Initial IPE analyses were confined to cross-field structure [2], [3]. We were able to show that the cross-field structure is characterized exclusively by a two-component inverse power law with $p_1 < p_2$. A systematic variation of the evolving structure parameters was identified as well. However, it is clear from Figure 1 that structure measured in vertical planes varies as the planes are rotated. The upper and middle frames of Figure 3 compare horizontal scans from the cross-field (right frame) and meriodinal plane (left frame) realizations shown in Figure 2. The intercepted cross-field scan subtends 150 km whereas the intercepted meridionall-plane scan subtends over 1000 km. The second and fourth frames in Figure 3 show the measured electron density SDFs (red). The overlaid green curves show two-component inverse power law SDFs,

$$\Phi_{N_e}(\kappa_y) = C_s \left\{ \begin{array}{ll} \kappa_y^{-p_1} & \text{for } \kappa_y \le \kappa_0 \\ \kappa_0^{p_2-p_1}\kappa_y^{p_2} & \text{for } \kappa_y > \kappa_0 \end{array} \right. , \qquad (1)$$

evaluated with IPE parameters. Because of field-line curvature meriodinal plane structure captures large scales, which are sparsely sampled in the equatorial plane and thereby not fully unresolved.

2 Imposed Magnetic Field Curvature Structure Variation

Ionospheric diagnostics respond to structure intercepted by a probe or integrated along a translating propagation path. Assuming the structure is invariant over a measurement interval, modeling or diagnostic interpretation follows

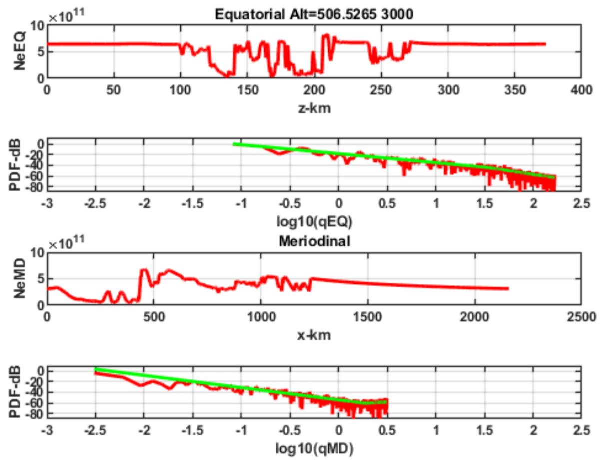

Figure 3: Upper frame shows horizontal scan of equatorial plane structure at 509 km (red). Second frame shows measured SDF (red) and IPE SDF overlaid (green). Lower frames summarize the larger span meridian plane structure.

from knowledge of the structure along a specified trajectory. To the extent that EPB simulations are representative of low-latitude ionospheric structure evolution, we expect developed local EPB structure to be characterized by striations intercepting the geomagnetic equatorial plane.

Potential striation paths can be determined by tracing the magnetic field from intercepted ionosphere penetration points. An altitude inflection identifies penetration of the equatorial plane where the structure is defined. The IGRF model defines eastward, northward, and downward components of the magnetic field at specified GPS (llh) locations. With a sign reversal the magnetic field vector is defined in a topocentric (tcs) system centered on the llh location. With alternating llh and tcs coordinate transformations the magnetic field can be traced along upward or downward directions from any GPS location. The downward traced fields intercept the surface. The upward traced field lines progress to an inflection point and return to the surface. A field-tracing algorithm was developed for exploration.

Penetration point trajectories representing constant altitude scans were generated with orientations varying from meriodinal to cross field alignment. Figure 4 shows a cross-field geometry. The green pentagrams identify selected trajectory samples. The traced field line intercepting the penetration point are shown in red. The single red pentagram is the station location. Blue pentagrams locate altitude inflection points in the equatorial plane. Figure 5 show a meriodinal trajectory. The sample spacing is compresses as the field lines from the equatorial plan map onto the trajectory. However, trajectories from stations displaced from the geomagnetic meridian typically do not connect to

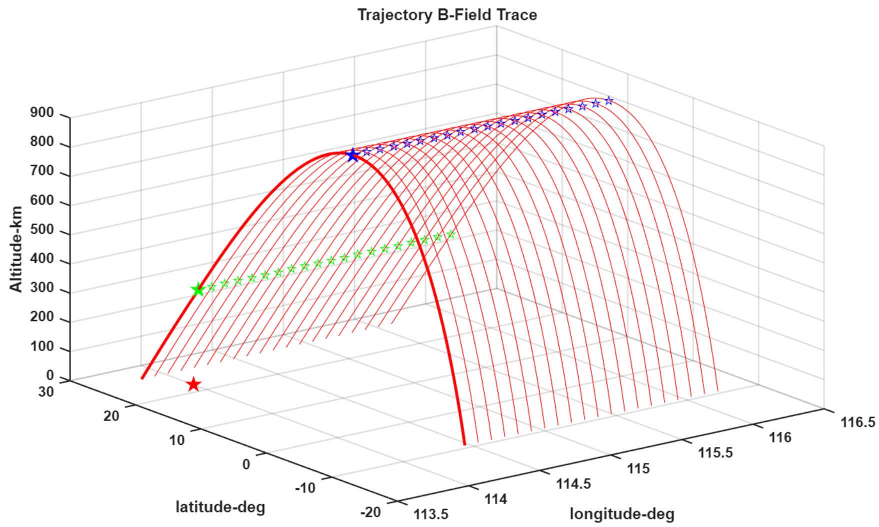

Figure 4: Field-line trajectories (red) from east-west penetration points identified by green pentagrams south of a Hong Kong station. Altitude inflection points are indicated by blue pentagrams.

the equatorial plane below 800 km. Figure 6 is shows an example.

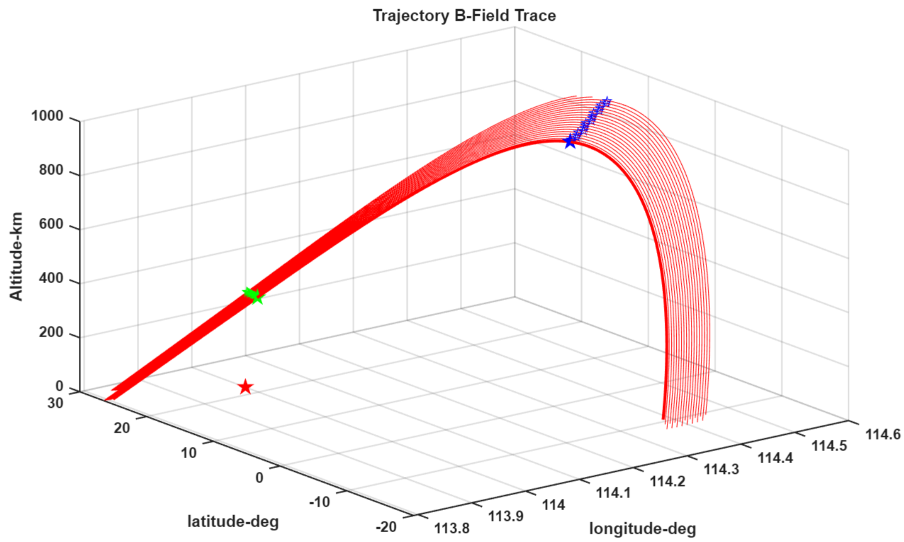

Figure 5: Field-line trajectories (red) from meridional penetration points identified by green pentagrams south of a Hong Kong station. Altitude inflection points are indicated by blue pentagrams.

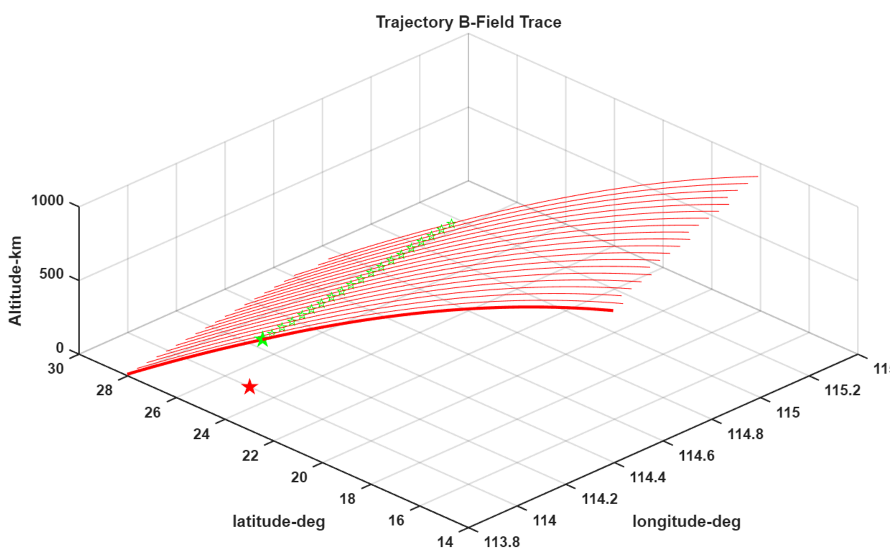

Figure 6: Field-line trajectories (red) from penetration points identified by green pentagrams south of a Hong Kong station. No altitude inflection points in structure altitude range.

We showed that configurations of parallel field-aligned striations can reproduce in expectation two-component inverse power law SDFs [4]. If the striations were constrained to follow true field lines the imposed structure change could be demonstrated. The characteristic $p_1 < p_2$ structure a sufficient condition for association with the EPB mechanism. However, structure evolution and/or departures from ideal EPB initial conditions must also be considered along with other structure mechanisms. The next section summarizes the observed structure characteristics and geometries from BP-IPE analysis of the GPS and GNSS data introduced in [5].

3 Low Latitude GPS/GNSS Structure Diagnostics Summary

Processed GPS data from Hong Kong over a one-year period from 2013 to 2014 and more recent GNSS data from stations at Lampedusa in the Mediterranean south of Italy and Malindi on the east coast of Africa as summarized in [5] were made available for this study. The data processing is described in *Diagnostic Processing Review*. Validation of the operations using MPS simulations is described in *Extended Phase Screen Model Review*. IPE-BP processing was applied to 5-min segments sampled at 100 Hz for GPS and 50 Hz for GNSS at two pre-selected frequencies. The full geometry, SNR, corrected penetration point height, IPE structure parameters, and v_{effBP} were retained for summary analysis. Structure parameters are accepted for diagnostic analysis only if the corrected penetration-point heights using the BP range lie between 200 and 800 km.

The following table summarizes the processed segments. The total number of segments that support estimates of $S4$, σ_ϕ, and $ROTI$ is listed for each station, Hong Kong 1159 segments, Lampedusa, 586 segments, and Malindi, 646. Suspected multi-path, interference is the primary reasons for rejecting data segments. The BP_OK rows in the table indicate the number of structure estimates by structure type. The EX_OK rows indicate the number of segments connected to equatorial plane intercepts below 800 km. Comparable numbers of BP_OK segments were classified P12 (single-component power law) and two-component power-law. Within the two-component category PPB structure segments significantly exceed the EPB structure segments.

Segment Structure Summary

	EPB	PPB	P12
Hong Kong 1159 segs			
BP_OK=722	95	234	393
EX_OK=193	43	57	93
Lampedusa 586 segs			
BP_OK= 324	7	109	208
EX_OK= 11	0	4	7
Malindi 646 segs			
BP_OK= 390	14	193	183
EX_OK= 377	14	193	183

Table 1

Figure 7 summarizes the Hong Kong BPO_OK parameters and the corrected penetration point height. The $p_2 - p_1$ difference is plotted in the second frame. Positive differences exclude the PPB structure. Negative differences exclude the EPB structure. The penetration point height is derived from the BP minimization range. We have found that using the BP-IPE parameters and Fresnel scale estimates to predict structure observables are generally in good agreement with measured values. This implies that a statistically equivalent phase screen is consistent with the intercepted structure. However, without calculating the theoretical value of $S4$ explicitly we know that theoretical predictions of $S4$ should vary monotonically with the universal strength parameter

$$U = C_P \begin{cases} \rho_F^{p_1-1} & \text{for } \mu_0 \leq 1 \\ \rho_F^{p_1-1} q_0^{p_1-p_2} & \text{for } \mu_0 \leq 1 \end{cases} . \tag{2}$$

Verifying that the median variation of measured $S4$ versus calculated U provides a consistence check. It also reveals definitive characteristics of the EPB, PPB, and P12 structure classes.

For example, the left frames in Figure 8 display measured Hong Kong $S4$ values plotted against U evaluated with measured structure and ρ_F parameters. The expected increase of $S4$ with increasing U is observed for each population. However, the unconstrained occurrence of U is different for each category. The U distribution associated with the single-index P12 segments are nearly uniform, whereas the U distribution associated with the PPB segments has a peak at lower U values. The U distribution associated with the EPB segments increases monotonically. These patterns can be reconciled with the strong dependence of scintillation intensity on the large-scale structure prominence implied by large p_1 values.

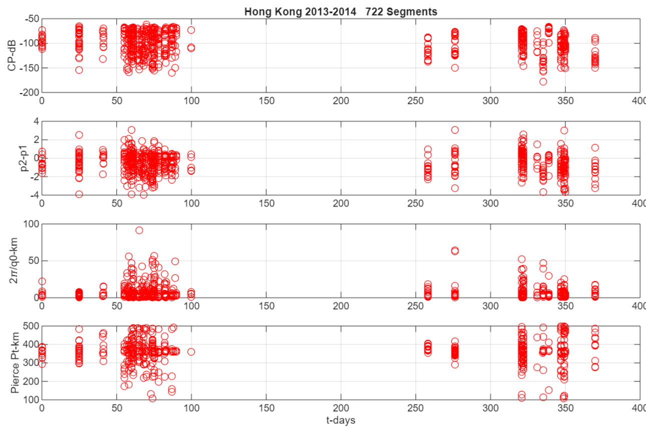

Figure 7: Summary of Hong Kong structure parameters (frames 1, 2, and 3) and pierce-point height (frame 4) plotted against days from 13-Oct-2019 14:16:00.

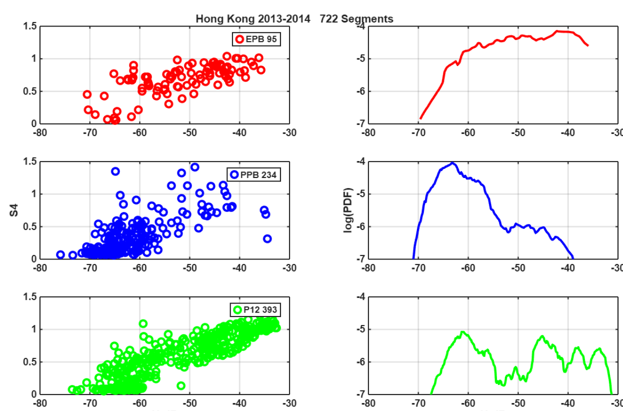

Figure 8: Left hand frames show $S4$ versus U plots for the EPB, PPB, and P12 segments. The right hand frames show the respective probability distributions of U

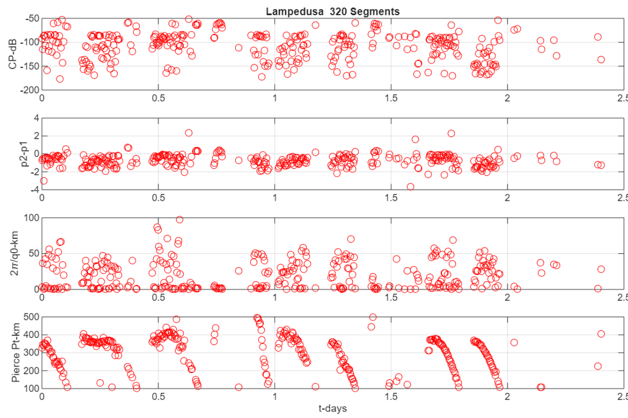

Figure 9: Summary of Lampedusa structure parameters (frames 1, 2, and 3) and pierce-point height (frame 4) plotted against days.

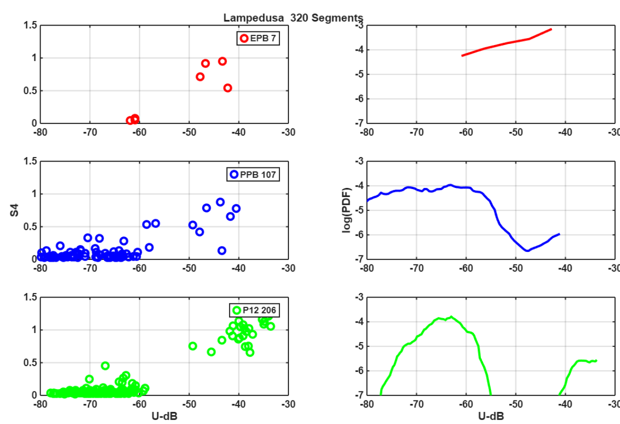

Figure 10: Left hand frames show $S4$ versus U plots for the EPB, PPB, and P12 segments. The right hand frames show the respective probability distributions of U, irrespective of $S4$.

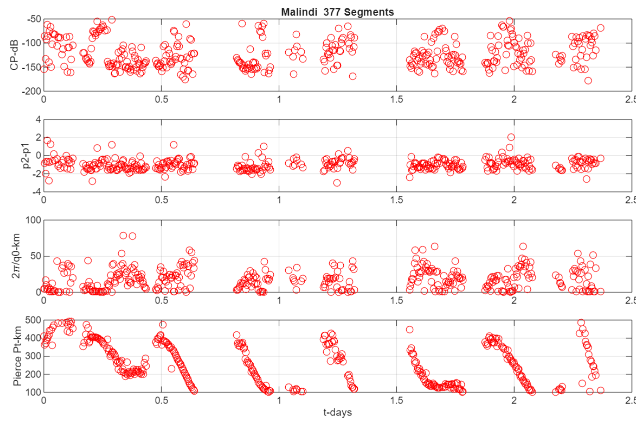

Figure 11: Summary of Malindi structure parameters (frames 1, 2, and 3) and pierce-point height (frame 4) plotted against days.

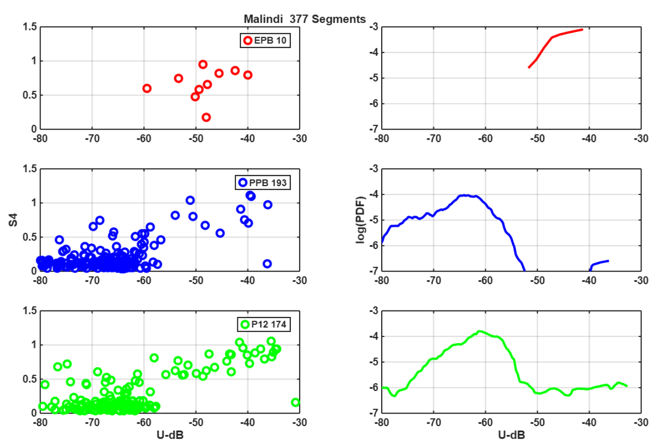

Figure 12: Left hand frames show $S4$ versus U plots for the EPB, PPB, and P12 segments. The right hand frames show the respective probability distributions of U

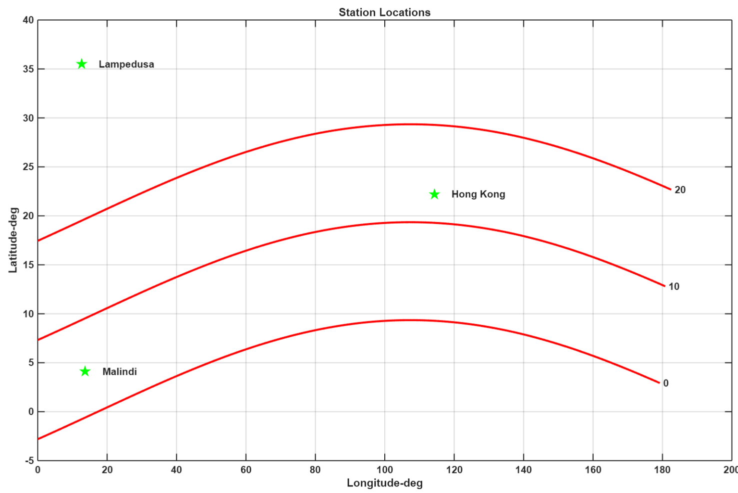

Figure 13: Geographic locations of GPS and GNSS stations, with surface magnetic field lines overlaid.

Figures 9 10 and Figures 11 12 respectively summarize the Lampedusa and Malindi data. Significant $S4$ occurrence is confined to the Lampedusa and Malindi trajectory segments entering or exiting the anomaly region at ~15 deg. latitude. The structure definition is not as definitive as for the Hong Kong data, although overall $S4$ versus U trends are as expected. The fact that very few Lampedusa and Malindi segments were classified as EPB structure may be due to the smaller number of structured segments. Otherwise, the Lampedusa and Malindi $S4$ occurrence patterns are remarkably similar. Systematic variations of the BP corrected penetration point heights are also similar. Figure 13 shows the locations of the stations relative to the geomagnetic equator. The Hong Kong station is in the equatorial anomaly region, whereas the Lampedusa and Malindi stations look into the anomaly region with the Malindi station nearly on the magnetic equator.

3.1 Parameter Interpretation

The development up to his point establishes that three categories of structure are being intercepted along the low-latitude propagation paths. Validated BP-IPE diagnostic parameters derived from low-latitude GNSS satellite 5-min segments acquired during periods of expected enhanced scintillation activity have been classified as EPB with $p_2 - p_1 > 0.5$, PPB with $p_1 - p_2 > 1$, or P12 with structure indistinguishable from a single inverse power law. Our working hypothesis is that the reconstructed phase from a back-propagated complex scintillation estimate captures the path-integrated structure. Necessary conditions are listed below:

1. The intercepted structure can be visualized as a random collection of elongated *magnetic-field-aligned* striations. The size distribution of the striations is defined by striation profile intersections with or containment within two-dimensional slice planes cutting across the striations. This implies that defining statistical measures are two-dimensional.

2. An evolving complex field intercepting the structure can be decomposed into a spectrum of plane waves that subtend a narrow range of propagation angles. Under this assumption multiple phase screen (MPS) simulations capture the essential propagation effects.

3. Processing is performed over segments with a predetermined length. The segment structure is characterized by statistical measures generated from samples within the segments. Sufficient homogeneity to support definitive statistical measures must verified.

4. The observed temporal structure is the result of incremental integration over a translating propagation path intercepting structure that evolves slowly enough to be spatially invariant over the measurement interval.

The interpretation of structure that meeds these assumptions is summarized in [5]. To the extent that the IPE structure parameters satisfy consistency requirements and assumptions 1 through 4 hold, measured structure parameters support statistically equivalent path-integrated in-situ structure.

3.2 Diagnostic Structure Summary

Assuming that each segment is responding to path-integrated structure, extended statistically homogeneous regions should appear as clusters. Figure 14 summarizes Hong Kong occurrence by pass of EPB and PPB segments. The largest PPB cluster had 16 segments, which occurred in the spring equinox period. The largest EPB cluster had 9 segments, which occurred fall equinox period . The EPB mechanism in isolation would be expected to produce a preponderance of EPB and P12 segments. PPB segments would be confined to regions where magnetic field lines from the equatorial plane intercepts converge as demonstrated in Section 2. The patterns in Figure 14 cannot be reconciled with ideal EPB structure evolution.

To explore the occurrence patterns, Figure 15 shows color coded penetration points (green pentagram=> EPB, green circle =>PPB, green asterisk=>P12) superimposed on the field lines (red). The altitude reversal indicating penetration of the geomagnetic equatorial plane is marked with a blue pentagram. A diagnostic tool was developed to explore the structure development details. The segment progression is from left to right. The time duration is one hour.

Figures 16 and 17 summarize structure details for segments captured during the initial phase of the pass. There progression is from strong P12 structure to moderate PPB structure. The upper left frames show the entire pass for reference. Time has been converted to distance. As described in *Diagnostic Processing Review*, a segment v_{BPeff} velocity for back propagation is derived for each segment. The lower left frame shows the measured and back propagated intensity. There is little change in $S4$. However, the back-propagated phase overlaid in red on the measured phase in the upper right frame is extracting the large scale structure albeit with phase jumps. The measured phase SDF with the theoretical SDF using the measured parameters overlaid verify the classification, namely P12 to PPB. Figures 18 and 19 sample the extended region of EPB structure.

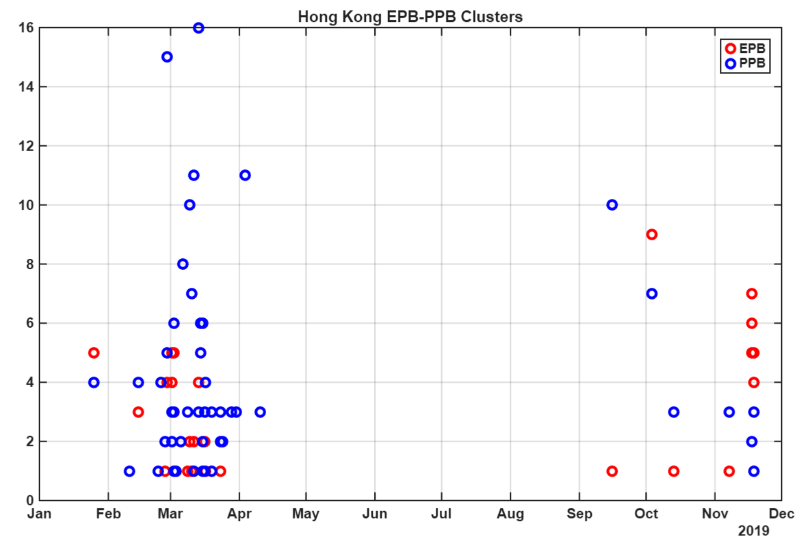

Figure 14: Hong Kong segment EPB (red) and PPB (blue) occurrence for each pass by date.

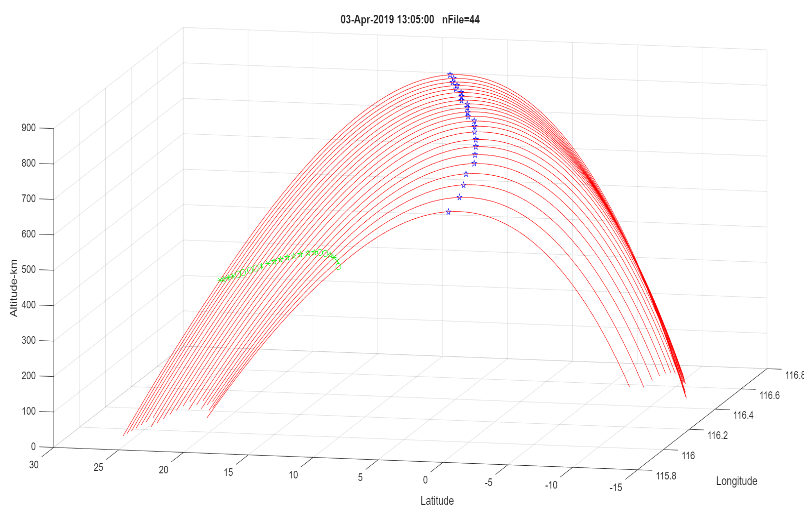

Figure 15: Pass 44 Field-line trace from green pierces points (pentagram=>EPB, circle=>PPB, asterisk=>P12). Blue pentagrams indicate equatorial plane intercepts.

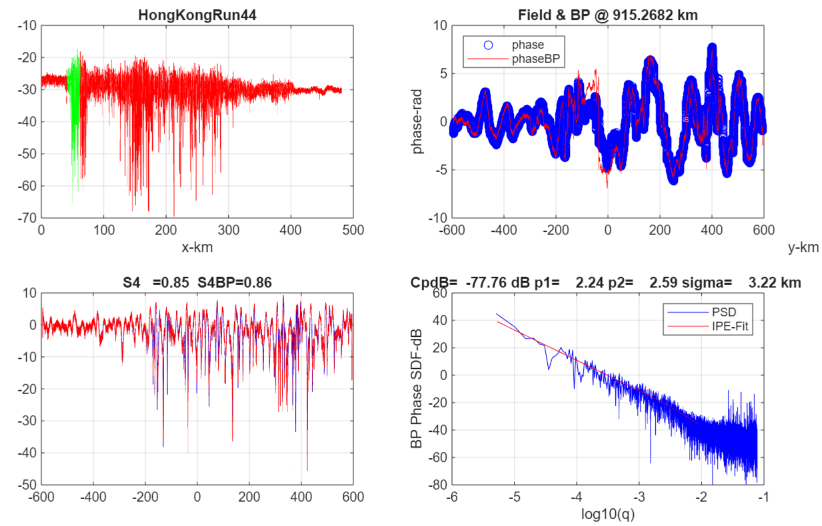

Figure 16: Segment structure summary. Upper left entire pass intensity (red) with segment highlighted (green). Right frame is segment phase before (blue) and after (red) back propagation. Lower right frame is measured (blue) SDF and theory (red). Lower left frames shows intensity associated with phase in upper right frame.

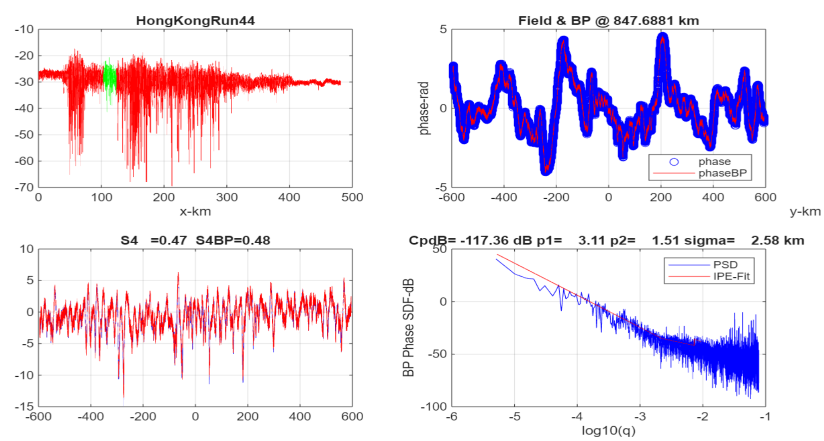

Figure 17: Segment structure summary. Upper left entire pass intensity (red) with segment highlighted (green). Right frame is segment phase before (blue) and after (red) back propagation. Lower right frame is measured (blue) SDF and theory (red). Lower left frames shows intensity associated with phase in upper right frame.

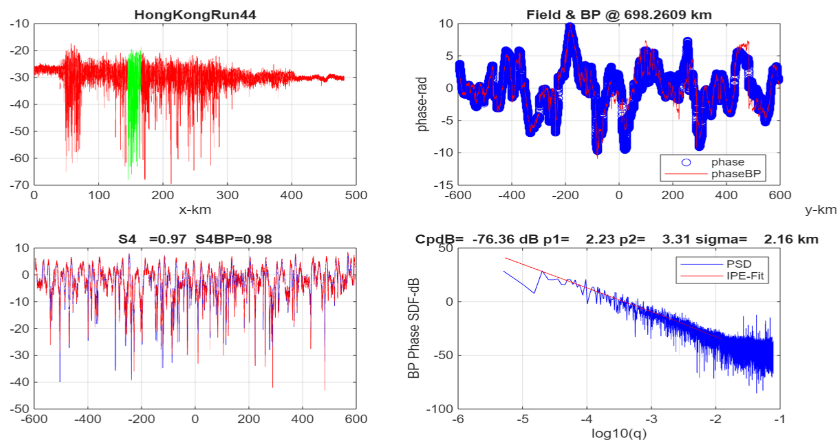

Figure 18: Segment structure summary. Upper left entire pass intensity (red) with segment highlighted (green). Right frame is segment phase before (blue) and after (red) back propagation. Lower right frame is measured (blue) SDF and theory (red). Lower left frames shows intensity associated with phase in upper right frame.

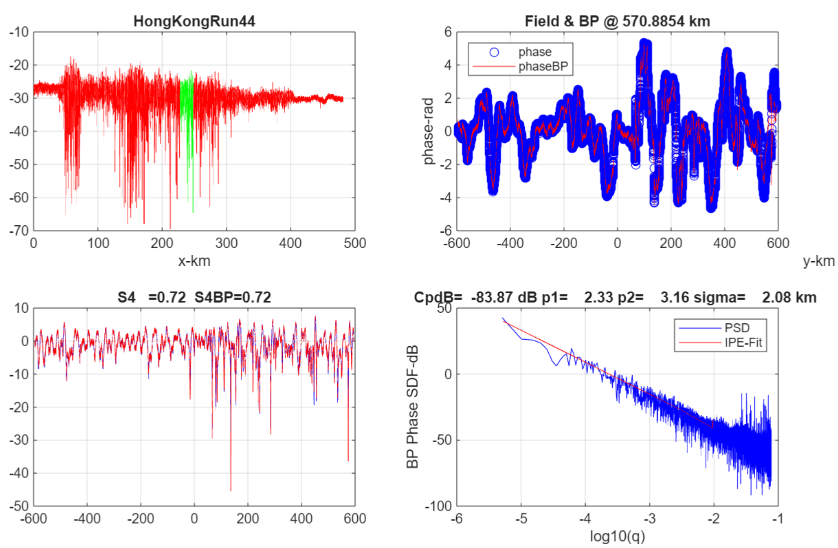

Figure 19: Segment structure summary. Upper left entire pass intensity (red) with segment highlighted (green). Right frame is segment phase before (blue) and after (red) back propagation. Lower right frame is measured (blue) SDF and theory (red). Lower left frames shows intensity associated with phase in upper right frame.

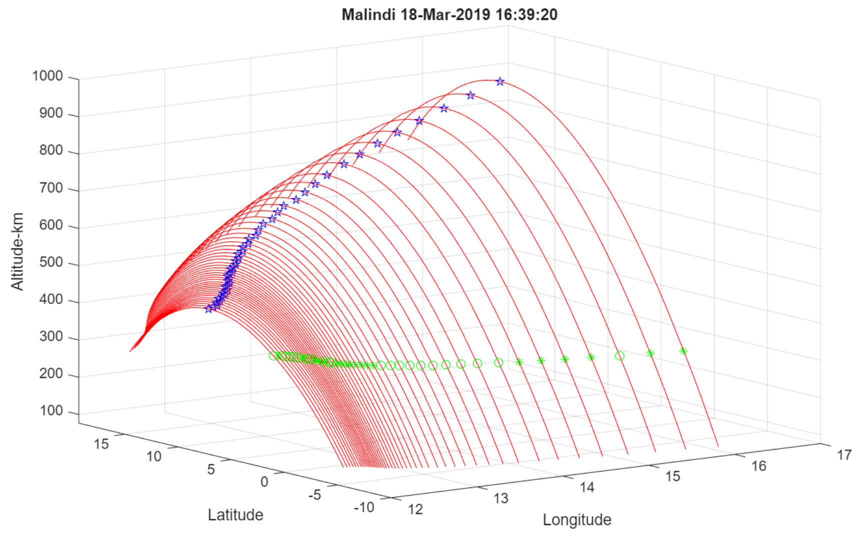

Figure 20: Malindi pass 3 Field-line trace from green pierces points (pentagram=>EPB, circle=>PPB, asterisk=>P12). Blue pentagrams indicate equatorial plane intercepts.

The Lampedusa and Malindi passes are dominated by PPB and P12 structure with very similar variations. The Malindi passes are particularly interesting because the station location nearly on the magnetic equator produces only favorable geometries. Figure 20 is an example. Figure 21 verifies the extreme PPB structure consistent with smaller turbulent strength parameters associated with extreme scintillation because of the large p_1 values.

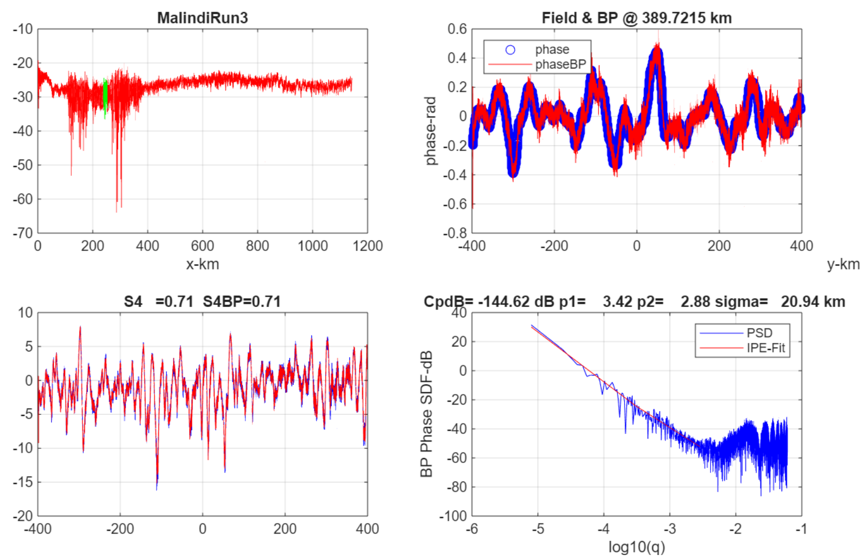

Figure 21: Segment structure summary. Upper left entire pass intensity (red) with segment highlighted (green). Right frame is segment phase before (blue) and after (red) back propagation. Lower right frame is measured (blue) SDF and theory (red). Lower left frames shows intensity associated with phase in upper right frame.

All of the GPS and GNSS segments, particularly segments with moderate to extreme scintillation show the same measurement consistency indicating that low-latitude scintillation generates structure that can be identified as one of three structure types. There is no immediate correlation with propagation geometry, which the exception that converging measurement pierce points precluded EPB structure. The fact that the GNSS data, which was acquired at the northern and souther boundaries of the anomaly region generally preclude EPB indicate that the structure development depends the state of the ionosphere.

4 Summary and Conclusions

This report summarized the interpretation of structure diagnostics derived from low-latitude GNSS scintillation. Upon applying IPE structure estimation to phase extracted from back-propagated complex scintillation estimates, we found 3 distinct two-component power-law structures, designated EPB with $p_2 - p_1 > 0$, P12 with $p_1\tilde{}p_2$, and PPB with $p_1 - p_2 > 0$. Although EPB structure evolves from the well established $E \times B$ instability initiated by a bottom side perturbation imposed on an otherwise uniform F-layer, it was the least-observed category. The consistency of the results indicate that the implied structure variation is reflecting intercepted structure.

The Back propagation method is robust, efficient. It does require time to space conversion. The assignment of v_{effBP} affects the scale range, which affects the identification of structure scales. With that caveat, Figures 16, 17, 18, 19, and 21 show significant structure contributions in the tens of kilometers range, which suggests traveling ionospheric disturbances. It may be that the structures have been overlooked because the weak scintillation theory emphasizes subkilometer structure. Additional measurements and structure simulations are needed to support the structure variation hypothesis.

References

[1] T Yokoyama. A review on the numerical simulation of equatorial plasma bubbles toward scintillation evaluation and forecasting. *Prog Earth Planet Sci*, 4, 2027. doi.org/10.1186/s40645-017-0153-6.

[2] C. L. Rino and C. S. Carrano. On the characterization of intermediate-scale ionospheric structure. *Radio Science*, 53, 2018. doi: 10.1029/2018RS006709.

[3] Charles Rino, Tatsuhiro Yokoyama, and Charles Carrano. A three dimensional stochastic structure model derived from high resolution isolated equatorial plasma bubble simulations. *Earth, Planets and Space Science*, 75, 2023. doi.org/10.1186/s40623-023-01823-6.

[4] C Rino, C. Carrano, K. Groves, and T. Yokoyama. A configuration space model for intermediate-scale ionospheric structure. *Radio Science*, 53, 2018. 10.1029/2018RS006678.

[5] Charles Rino, Charles Carrano, Dmytro Vasylyev, Theodore Beach, Brian Breitsch, Yu Morton, and Keith Groves. Extreme scintillation structure diagnostics. *Journal of Atmospheric and Solar Terrestial Physics*, 282, 2026. https://doi.org/10.1016/j.jastp.2026.106805.